Japanese Journal of Applied Physics
Vol. 47, No. 5, 2008, pp. 4155–4164

Automated Segmentation of Heart Wall Using Coherence Among Ultrasonic RF Echoes

Takaomi KINUGAWA, Hideyuki HASEGAWA, and Hiroshi KANAI*

Graduate School of Engineering, Tohoku University, Sendai 980-8579, Japan

(Received November 22, 2007; revised February 1, 2008; accepted February 12, 2008; published online May 23, 2008)

In conventional ultrasonic tomographic images, the heart wall cannot be distinguished from the cardiac lumen automatically on the basis of only the echogenicity. One of the biggest problems is that echogenicity, which corresponds to the amplitude of an RF echo, in the heart wall is as low as that in the lumen. In this study, ultrasonic RF echoes from the heart wall and lumen were analyzed in the frequency domain in order to distinguish the heart wall from the lumen automatically. Temporal changes in complex frequency spectra were evaluated using the magnitude-squared coherence function. The coherence function of RF signals scattered from the interventricular septum (IVS) was high. In contrast, the coherence function in the right ventricle (RV) and left ventricle (LV) was low because the scatterers (blood cells) slipped off from the focal area of the ultrasonic beam by blood flow. For automated identification of the heart wall using the coherence function, the optimal threshold $T_0(f)$ for the coherence function should be determined. In this study, on the basis of the Bayes decision rule, the optimum value of $T_0(f)$ was determined. The coherence function of the region near the anterior wall in the RV was as high as that in the IVS because there are artifacts in the region near the anterior wall owing to echoes from the external tissue resulting from the sidelobe. However, the artifacts can be reduced by removing the stationary component from RF echoes before evaluating the coherence function. *In vivo* experimental results show that the differentiation of the heart wall from the lumen was improved significantly using the proposed method. [DOI: 10.1143/JJAP.47.4155]

KEYWORDS: ultrasonic RF echo, heart, region identification, frequency analysis, coherence function

1. Introduction

In recent years, the number of patients suffering from cardiovascular diseases such as cardiac infarction has increased. Cardiac catheterization, X-ray imaging, computerized tomography (CT), magnetic resonance imaging (MRI), and ultrasonography are employed for diagnosis of these diseases.[1)] Among these methods, ultrasonography is superior to the others in terms of noninvasive and real-time diagnosis. In addition to the morphological diagnosis of the heart, identification of the heart wall is important for the evaluation of myocardial function[2–4)] because the region (= heart wall) to be analyzed must be determined.

In conventional ultrasonic tomographic images, the heart wall cannot be distinguished from the cardiac lumen automatically using only echogenicity. One of the biggest problems is that echogenicity, which corresponds to the amplitude of the RF echo, in the heart wall is as low as that in the lumen. Moreover, in the ultrasonic tomographic images of the heart, there are many artifacts due to the reflection of sidelobes by the external tissue such as ribs. Under these circumstances, in the conventional manual segmentation of the heart walls in B-mode images, the region of the heart wall is subjectively distinguished from the lumen on the basis of the *a priori* knowledge about the heart structure.

Nillesen *et al.* reduced the overlap between brightnesses in the heart wall and lumen from 35.4 to 19.6% by smoothing brightness in each local region of interest in ultrasonic tomographic images.[5)] However, this method is not effective in the region with a low echo level inside the heart wall, and the heart wall is not completely distinguished from the lumen.

On the other hand, the frequency characteristics of RF echoes contain more information (amplitude and phase at each frequency) on echoes from scatterers in comparison with echo amplitudes as long as signal-to-noise ratio (S/N) is not too small. Therefore, there is a possibility that the lumen and heart wall whose echogenicities are similar can be differentiated using the frequency characteristics of RF echoes from them. Lizzi *et al.* estimated the effective diameter of an ultrasonic scatterer on the basis of the slope and intercept of the power spectrum normalized by that of the echo from the flat plate.[6,7)] Watson *et al.* and Waters *et al.* classified arterial plaques *in vitro* on the basis of the slope of a normalized power spectrum.[8,9)] Hall *et al.* evaluated the anisotropy of the frequency dependence of backscatters in the human myocardium.[10)] Georgia *et al.* characterized breast tissue on the basis of time-frequency analysis of RF signals.[11,12)] In this study, complex frequency spectra of echoes from the heart wall and lumen were analyzed for the automated identification of those regions.

2. Experimental Methods

2.1 Temporal changes in complex spectra of RF echoes

In this study, we focus on the difference between temporal changes in complex frequency spectra of RF echoes from the heart wall and the lumen. As shown in Fig. 1, in the heart wall, the phase changes of RF echoes during a few milliseconds [1.69 ms (1 frame), 3.38 ms (2 frames), ...] are very small when the motion of the myocardium is tracked (compensated) because the myocardium stays in the focal area of the ultrasonic beam, whereas small phase changes occur owing to a change in the thickness of myocardia. On the other hand, in the lumen, the motion of scatterers cannot be compensated because blood cells slip off from the focal area of the ultrasonic beam by blood flow. Therefore, phases of echoes would change even during a few milliseconds. In this study, the magnitude-squared coherence function was employed for evaluating this difference in variance in phase changes of RF echoes.

2.2 RF data acquisition

As illustrated in Fig. 2(a), the interventricular septum (IVS), right ventricle (RV), and left ventricle (LV) were scanned by an ultrasonic beam, which scans sparsely to

*E-mail address: hkanai@ecei.tohoku.ac.jp

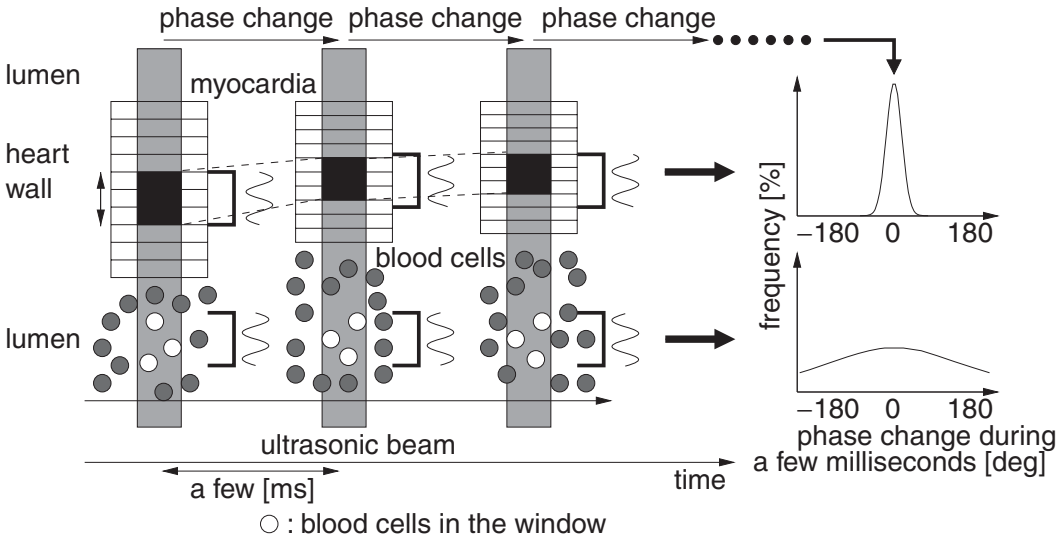

Fig. 1. Schematic diagram showing difference between phase changes of reflected waves during a few milliseconds in heart wall and lumen.

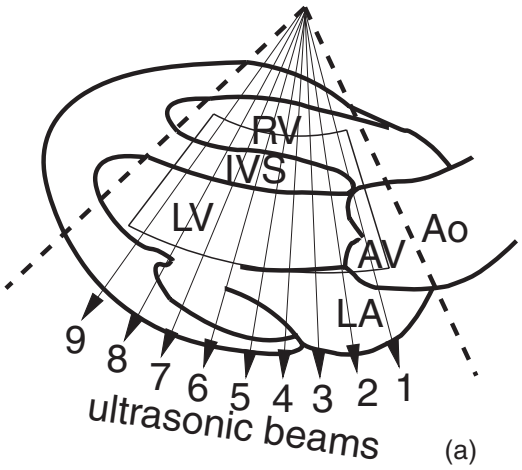

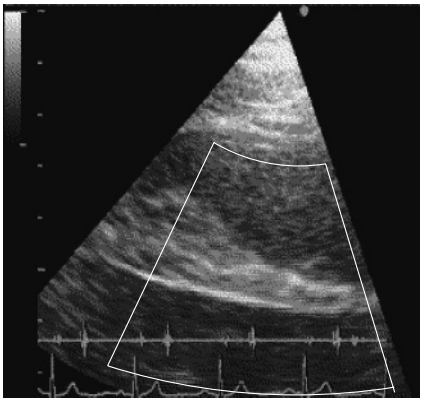

Fig. 2. (a) Illustration of tomographic view of human heart. (b) B-mode image of human heart in its longitudinal-axis view. Arrows in (a) show ultrasonic beams and the region surrounded by the line in (a) and (b) shows the acquisition area of RF signals.

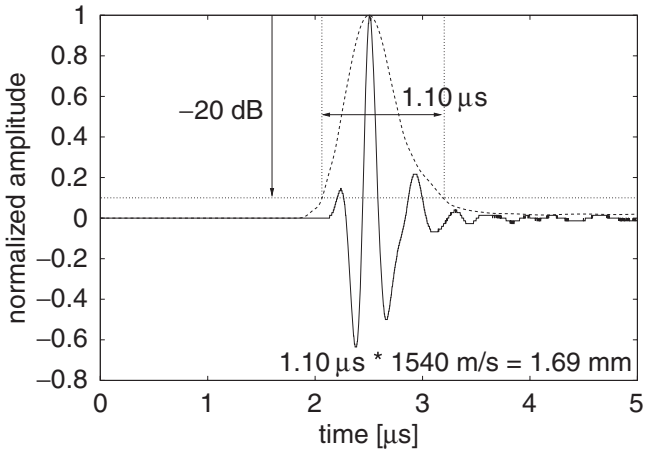

Fig. 3. Waveform of input ultrasonic pulse measured using hydrophone.

realize a high temporal resolution in a wide area.[3,13] First, RF data $\{y_n(x)\}$ along each of nine beams were acquired using a 3.75 MHz sector-type probe of ultrasonic diagnostic equipment (ALOKA SSD-6500), where n and x are frame (time) and depth, respectively. The sampling frequency of the RF signal was 15 MHz and the frame rate in the measurement was 592 Hz. Each RF data $y_n(x)$ contains a small bias signal owing to the ultrasonic diagnostic equipment. The bias should be removed because the direct current is out of band. The bias is not constant along the direction of depth and is removed in every short period $(K+1)\Delta x$ as follows:

$$\hat{y}_n(x) = y_n(x) - \frac{1}{K+1}\sum_{i=-K/2}^{K/2} y_n(x+i\Delta x), \qquad (2.1)$$

where $\hat{y}_n(x)$ is the RF signal after removing the regional bias and Δx is the sampling interval (= 51.3 µm) in the direction of depth. The number $K+1$ of the sampled points used for averaging is set to be 33 (1.69 mm) by referring to a pulse length of insonified ultrasound (width at −20 dB of the maximum of the envelope) of 1.69 mm in the soft tissue (sound velocity: 1540 m/s), as shown in Fig. 3.

2.3 *Artifact reduction*

RF data $\{y_n(x)\}$ contain the components of echoes from the external tissue such as ribs owing to sidelobes which

result in stationary artifacts. The artifact component was reduced using the feature that the external tissue does not move markedly with time as follows:

$$\tilde{y}_n(x) = \hat{y}_n(x) - \frac{1}{L+1}\sum_{i=-L/2}^{L/2} \hat{y}_{n+i}(x), \tag{2.2}$$

where $\tilde{y}_n(x)$ is the RF signal after artifact reduction. The mean absolute velocity of the myocardia in the IVS was 11 mm/s. When myocardia in the IVS displace over one ultrasonic wavelength ($\lambda = 513\,\mu$m) during $L+1$ frames, eq. (2.2) does not affect echoes from the heart wall markedly because the phase of $\hat{y}_x(n)$ rotates over 360° during $L+1$ frames and the second term in the right hand side of eq. (2.2) for the fluctuating component is close to zero in comparison with that for the stationary component. Therefore, $L+1$ should be set at a value larger than 13.8 [corresponding to a period of $(\lambda/2)/11\,\text{mm/s} = 23.3\,\text{ms}$] (condition 1). The wavelength of λ 513 µm is derived from sound velocity (= 1540 m/s) divided by the center frequency (3 MHz) of the insonified pulse shown in Fig. 3 and the two-way propagation of the ultrasound pulse between the probe and the object is considered. However, the artifact component also displaces toward the surface of the body by a mean velocity of 1.2 mm/s in the data shown in Fig. 2. Therefore, $L+1$ should be set as small as possible in order to reduce the artifact component effectively (condition 2). Consequently, $L+1$ was set to be 15 (25 ms) as the solution of the trade-off problem between conditions 1 and 2. The mean displacement of the artifact component in $L+1$ frames is suppressed to 30 µm (about 1/10 of the wavelength) when $L+1$ is 15. Therefore, the artifact component can be reduced sufficiently and the reduction of the other components is suppressed.

2.4 *Estimation of complex frequency spectrum*

The complex frequency spectrum $Y_{n,x}(f)$ in each frame n and at each depth x was estimated by applying the short-time Fourier transform to the RF signal $\tilde{y}_n(x)$ using a Hanning window. The window length was set at 1.64 mm (32 sampled points) by referring to an insonified ultrasonic pulse length of 1.69 mm in the soft tissue (sound velocity: 1540 m/s), as shown in Fig. 3. Then, the temporal changes of the spectra were analyzed by applying the short-time Fourier transform to multiple frames. The window position was moved so as to follow the motion of a point of interest using the *phased tracking method*[4,14] in order to realize the analysis of the same scatterers during 100 frames, and the spectra $\{Y_{n,x}(f)\}$ in 100 frames were obtained for each position x. Using the *phased tracking method*, the motion of a point of interest is traced without constraint of the sampling interval Δx along the depth direction, and the displacement of the point between two adjacent frames is obtained as a continuous value. However, the window position should be assigned to a discrete value depending on the sampling interval Δx. This difference $\delta x_{n,x}$ between the estimated position of the point of interest and the discrete position of the window leads to the undesirable phase shift $\delta\theta_{n,x}(f)$ between the estimated spectra, $Y_{n,x}(f)$ and $Y_{n+1,x}(f)$. This phase difference $\delta\theta_{n,x}(f)$ is given by

$$\delta\theta_{n,x}(f) = \frac{4\pi f}{c_0}\,\delta x_{n,x}, \tag{2.3}$$

where c_0 is the sound velocity of 1540 m/s. Consequently, $\delta\theta_{n,x}(f)$ can be compensated as follows:

$$\hat{Y}_{n,x}(f) = Y_{n,x}(f)e^{-j\delta\theta_{n,x}(f)}, \tag{2.4}$$

where $\hat{Y}_{n,x}(f)$ is the phase-corrected complex frequency spectrum.

2.5 *Estimation of coherence function*

Using the frequency spectrum $\hat{Y}_{n,x}(f)$ in each frame, the power of the time (frame) averaged frequency spectra $|\mathrm{E}_n[\hat{Y}_{n,x}(f)]|^2$ was obtained. In addition, the magnitude-squared coherence function (MSCF) $|\gamma_x(f)|^2$ was evaluated as follows:

$$|\gamma_x(f)|^2 = \frac{|\mathrm{E}_n[\hat{Y}^*_{2n,x}(f)\hat{Y}_{2n+N,x}(f)]|^2}{\mathrm{E}_n[|\hat{Y}_{2n,x}(f)|^2]\mathrm{E}_n[|\hat{Y}_{2n+N,x}(f)|^2]}, \quad (N = 1, 2, \ldots), \tag{2.5}$$

where $\mathrm{E}_n[\cdot]$ and $*$ are the time (frame) averaging during 100 frames and complex conjugate, respectively. The MSCF is a function for evaluating the difference between the characteristics of phase changes of echoes from the heart wall and the lumen as described in §2.1. In the numerator of eq. (2.5), the absolute value is taken after calculation of the mean of complex cross-spectra. By this operation, the variance in temporal changes in the complex spectra between two RF signals in $(2n)$-th and $(2n+N)$-th frames during 100 frames at each frequency is evaluated, i.e., the changes in phases of complex spectra significantly affect this averaging operation. The MSCF $|\gamma_x(f)|^2$ evaluates such change regardless of the amplitude of RF echoes as long as S/N is not small because it is normalized by the powers $\mathrm{E}_n[|\hat{Y}_{2n,x}(f)|^2]$ and $\mathrm{E}_n[|\hat{Y}_{2n+N,x}(f)|^2]$. In eq. (2.5), RF signals in $(2n)$-th and $(2n+N)$-th frames were used to reduce computation time because the MSCF between two RF signals in $(2n)$-th and $(2n+N)$-th frames is nearly the same as that between two RF signals in $(2n+1)$-th and $(2n+1+N)$-th frames because of the employed high frame rate. Although the method of region identification using brightness, in which the phase of an echo is not evaluated, was proposed,[5] our proposed method using complex spectra, which contain both amplitude and phase, is more suitable for region identification.

2.6 *Determination of optimal threshold for MSCF*

For the automated identification of the heart wall using the MSCF $|\gamma_x(f)|^2$, the optimal threshold level $T_0(f)$ for the MSCF was determined on the basis of the Bayes decision rule.[15,16] The *a posteriori* probability $P(\Omega_i \mid |\gamma_x(f)|^2)$, which shows the probability that $|\gamma_x(f)|^2$ belongs to the class Ω_i, is shown as follows:

$$P(\Omega_1 \mid |\gamma_x(f)|^2) \gtrless P(\Omega_2 \mid |\gamma_x(f)|^2) \rightarrow |\gamma_x(f)|^2 \in \begin{cases} \Omega_1 \\ \Omega_2 \end{cases}, \tag{2.6}$$

where the two classes Ω_1 and Ω_2 are the heart wall and the lumen, respectively. Using Bayes' theorem, the *a posteriori* probability $P(\Omega_i \mid |\gamma_x(f)|^2)$ is shown as follows:

$$P(\Omega_i \mid |\gamma_x(f)|^2) = \frac{p(|\gamma_x(f)|^2 \mid \Omega_i)P(\Omega_i)}{p(|\gamma_x(f)|^2)} \quad (i = 1, 2), \tag{2.7}$$

where $p(|\gamma_x(f)|^2)$, $P(\Omega_i)$, and $p(|\gamma_x(f)|^2 \mid \Omega_i)$ are the probability of occurrence of $|\gamma_x(f)|^2$, *a priori* probability

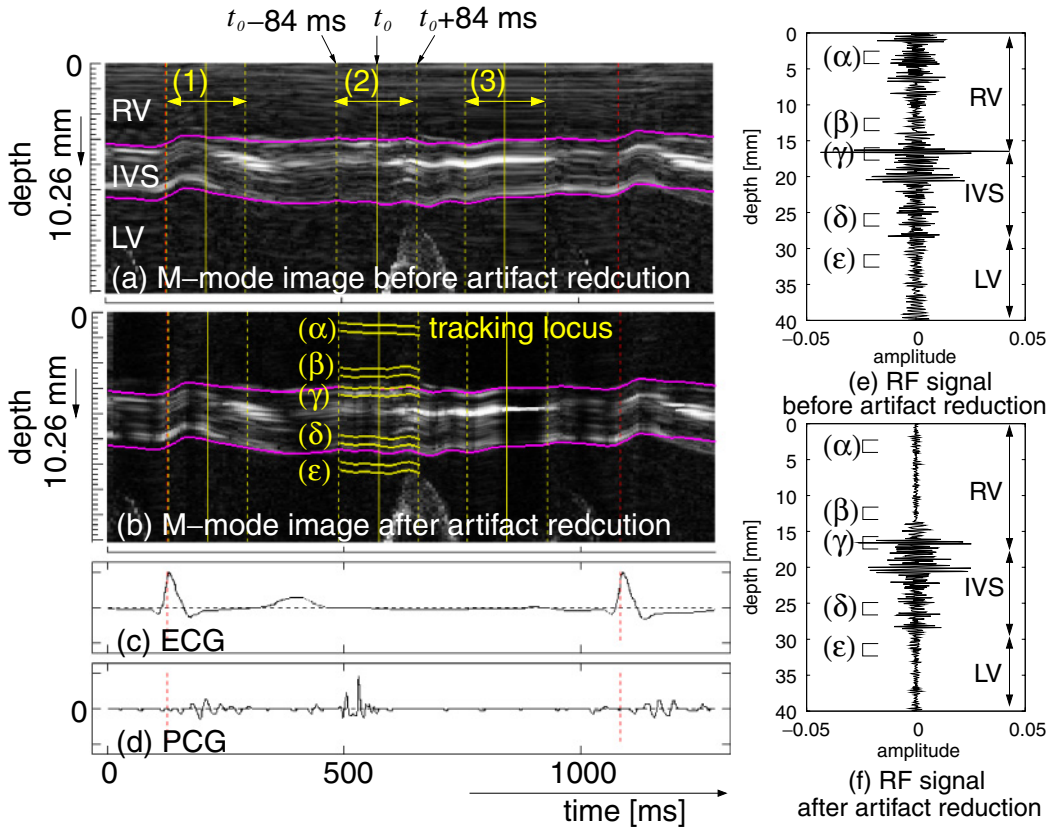

Fig. 4. (Color online) (a) M-mode image of heart along beam 5 shown in Fig. 2(a) before artifact reduction. (b) M-mode image of heart along beam 5 after artifact reduction. (c) Electrocardiogram (ECG). (d) Phonocardiogram (PCG). (e) RF signal $\hat{y}_{n_0}(x)$ in rapid filling phase before artifact reduction. (f) RF signal $\tilde{y}_{n_0}(x)$ in rapid filling phase after artifact reduction.

showing the occurrence of class Ω_i, and the conditional probability density function showing the occurrence of $|\gamma_x(f)|^2$ belonging to class Ω_i, respectively. By substituting eq. (2.7) into eq. (2.6), the following eq. (2.8) is derived.

$$p(|\gamma_x(f)|^2 \mid \Omega_1)P(\Omega_1) \gtrless p(|\gamma_x(f)|^2 \mid \Omega_2)P(\Omega_2)$$
$$\rightarrow |\gamma_x(f)|^2 \in \begin{cases} \Omega_1 \\ \Omega_2 \end{cases}. \tag{2.8}$$

In this study, the conditional probability density function $p(|\gamma_x(f)|^2 \mid \Omega_i)$ and *a priori* probability $P(\Omega_i)$ were calculated on the basis of the histograms of $|\gamma_x(f)|^2$ of the heart wall and lumen, which had been manually segmented. Using eq. (2.8), we determined the optimal threshold $T_0(f)$ for $|\gamma_x(f)|^2$.

3. *In vivo* Experimental Results

3.1 *RF data acquisition*

RF data were acquired from the heart of a healthy 25-year-old male, and the analysis described in the previous section was applied.

Figure 2(b) shows a B-mode image. RF data were obtained for the nine beams indicated by the arrows within the acquisition area surrounded by the line in Fig. 2(a).

Figures 4(a) and 4(b) show M-mode images along beam 5 before and after artifact reduction, respectively. Figures 4(c) and 4(d) show the electrocardiogram (ECG) and phonocardiogram (PCG), respectively. The stationary artifacts in the region (α) near the anterior wall shown in Fig. 4(a) were reduced, as shown in Fig. 4(b). The central time in the analyzing period t_0 was set so that it corresponds to one of three cardiac phases: (1) ejection, (2) rapid filling, and (3) reduced filling. RF data were analyzed around t_0 from $t_0 - 84$ to $t_0 + 84$ ms. The RF signals $\hat{y}_{n_0}(x)$ and $\tilde{y}_{n_0}(x)$, which are respectively before and after artifact reduction, at t_0 (= frame n_0) in the rapid filling phase are shown in Figs. 4(e) and 4(f), respectively. The amplitude of the RF signal in the region (α) near the anterior wall decreased after artifact reduction, as shown in Figs. 4(e) and 4(f). The instantaneous position of each point of interest estimated by the *phased tracking method* is indicated in Fig. 4(b) by the yellow lines of (α), (β), (γ), (δ), and (ε).

Regions (α), (β), (γ), (δ), and (ε) in Figs. 4(b) and 4(f) are the positions of windows for RV (near the anterior wall), RV, IVS (hyperechoic), IVS (hypoechoic), and LV, respectively. These five regions were chosen to compare the characteristics of echoes from the heart wall and lumen. Note that the amplitudes of RF signals in regions (β), (δ), and (ε) were similarly low. Figures 5(a) and 5(b) show the histograms of brightness $\hat{b}_n(x)$ and $\tilde{b}_n(x)$ before and after artifact reduction, normalized by their maximum values, in the heart wall and lumen acquired from nine beams shown in Fig. 2(a), respectively. The brightness $b_n(x)$ is defined as the common logarithm of the envelope of the RF signal as follows:

$$b_n(x) = \log\{\mathrm{LPF}[(y_n(x))^2]\}, \tag{3.1}$$

where LPF[·] shows the low-pass filtering. The overlap of brightness $\hat{b}_n(x)$ between the heart wall and lumen was

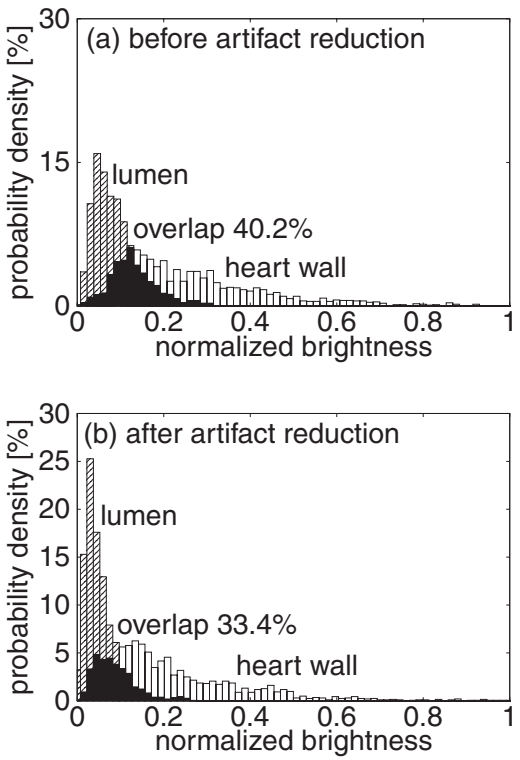

Fig. 5. Histograms of brightness in heart wall and lumen acquired from 9 beams (a) before and (b) after artifact reduction. In this analysis, the region near the anterior wall (<10.26 mm), in which the artifact was dominant, was not included.

40.2% before artifact reduction. After artifact reduction, the overlap of brightness $\tilde{b}_n(x)$ was 33.4%. These large overlaps show that region identification of the heart wall using the brightness is difficult.

3.2 *Estimation of complex frequency spectrum and coherence function*

Figures 6(1-a) and 6(2-a) show the three instantaneous power spectra $|\hat{Y}_{n,x}(f)|^2$ and the power of the time-averaged complex spectrum $|\mathrm{E}_n[\hat{Y}_{n,x}(f)]|^2$ along beam 5 before and after artifact reduction, respectively, which were acquired from the regions (α) to (ε) in the rapid filling phase shown in Fig. 4(b). The shape of the power spectra changed with time even when the same region was analyzed. However, almost all the power spectra and power of the temporally averaged power spectra had the peaks at about 2 MHz ($\equiv f_\mathrm{p}$) and also had the other peaks at $2f_\mathrm{p}$. In region (β) in RV, except for the region near the anterior wall, and in region (ε) in LV, the power of the averaged complex spectra was lower than the instantaneous power spectra by 10 to 20 dB. Particularly in the high-frequency range ($= 2f_\mathrm{p}$), the decrease in power of the averaged complex spectra in the lumen was marked. In the IVS [regions (γ) and (δ)], however, the power of the averaged spectra was similar to that of the instantaneous spectra.

Figures 6(1-b) and 6(2-b) show the MSCF $|\gamma_x(f)|^2$ obtained during the period $t_0 - 84 \le t \le t_0 + 84$ ms in the rapid filling phase at each depth x along beam 5 before and after artifact reduction, respectively. In Fig. 6(b), the frame intervals N between two frames for the evaluation of correlation are 1 (1.69 ms) and 2 (3.38 ms). The MSCF of the RF echo scattered from the IVS was high. In contrast, the MSCF in the lumen was low because the scatterers (blood cells) slipped off from the focal area of the ultrasonic beam caused by blood flow. As shown in Fig. 6(2-b), in the heart wall, the MSCF in the frequency range $2f_\mathrm{p}$ was as high as that in f_p. On the other hand, in the lumen, the MSCF in the frequency range $2f_\mathrm{p}$ was lower than that in f_p.

Figure 7(a) shows the original B-mode image. Figure 7(b) shows the MSCF $|\gamma_x(f)|^2$ in multiple frames in three cardiac phases. In Fig. 7(b), the frame intervals N between two frames for the evaluation of correlation are 1 (1.69 ms) and 2 (3.38 ms). In every cardiac phase, the MSCF in the heart wall was higher than that in the lumen.

The MSCF in the RV-lumen region (α) near the anterior wall in Fig. 6(1-b) was as high as that in the IVS because the artifact, which did not move markedly with time, was dominant in this region. In contrast, in Fig. 6(2-b), the MSCF in the region (α) near the anterior wall was reduced using artifact reduction in eq. (2.2). However, the MSCF in the heart wall did not change markedly between before and after artifact reduction, as shown in Figs. 6(1-b) and 6(2-b). Therefore, it was shown that eq. (2.2) was the appropriate preprocessing for region identification using the MSCF because artifact reduction did not affect the other echo components significantly.

3.3 *Region identification using MSCF*

As shown in Fig. 5(b), the overlap of brightnesses $\tilde{b}_n(x)$ between the heart wall and lumen was too large for differentiation of the heart wall from the lumen using brightness. On the other hand, as shown in Fig. 8, the overlap (%overlap) of the MSCF $|\gamma_x(f)|^2$ was only 3.0% in the rapid filling phase at 4.2 MHz. These histograms correspond to probability density functions $\{p(|\gamma_x(f)|^2 \mid \Omega_i)\}$ $(i = 1, 2)$ and the %overlap shows the probability of misclassification when using eq. (2.8). In these analyses shown in Figs. 5 and 8, the region (α) near the anterior wall (<10.26 mm), in which the artifact was dominant, was not included in order to determine the optimal threshold $T_0(f)$ for the MSCF. Figure 9(a) shows the %overlap of the MSCF between the heart wall and the lumen in three cardiac phases. The overlap of the MSCF at the frequency $2f_\mathrm{p}$ ($\equiv 4$ MHz) was slightly smaller than that at f_p ($\equiv 2$ MHz) and the overlap was the smallest when $N = 1$. Therefore, the frequency $2f_\mathrm{p}$ and $N = 1$ were employed in the following region identification.

On the basis of eq. (2.8), we determined the optimal threshold $T_0(f)$ for the MSCF, as shown in Fig. 9(b). Subsequently, the results of region identification are shown in Fig. 10, where the regions shown in red are identified as the heart wall and those shown in blue are identified as the lumen. In this figure, white lines show the manually determined boundary between IVS and ventricles. These lines are determined by referring to the leading edges of RF echoes from interfaces. Although there were misclassifications around the boundary between IVS and ventricles because the analyzed window has a width of 1.64 mm, the IVS is clearly differentiated from the RV and the LV in all cardiac phases, and the opening and closing of the aortic valve (AV) can also be observed in Fig. 10.

The same procedure was applied to another subject

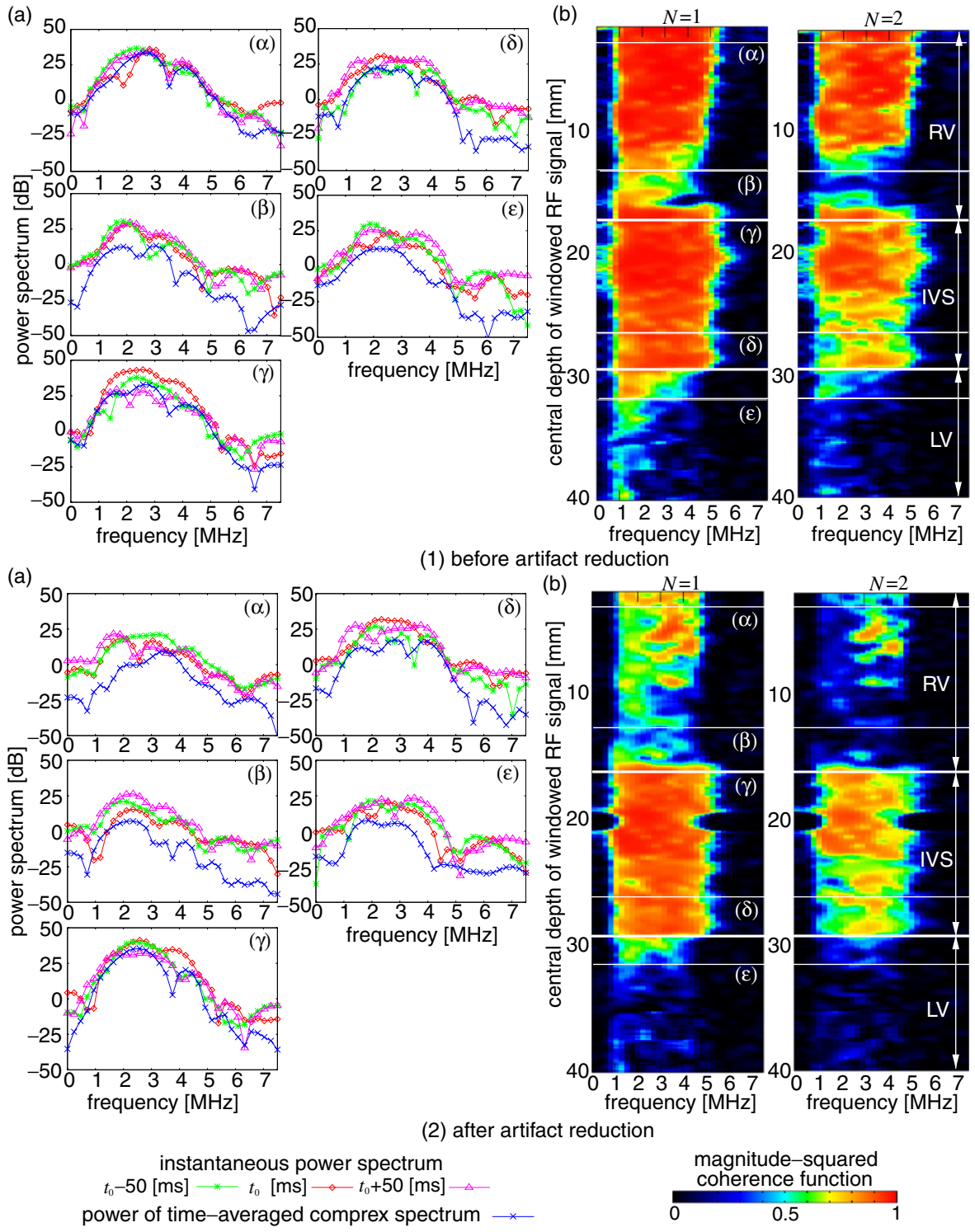

Fig. 6. (Color online) (a) Power spectra $|\hat{Y}_{n,x}(f)|^2$ of RF signal along beam 5 and power of time-averaged complex spectrum $|\mathrm{E}_n[\hat{Y}_{n,x}(f)]|^2$. (b) MSCF $|\gamma_x(f)|^2$ between spectra in $2n$-th and $(2n+N)$-th frames along beam 5. (1) Before artifact reduction. (2) After artifact reduction.

(healthy 24-year-old male) in the rapid filling phase. Figure 11(a) shows the original B-mode image. The brightness inside IVS was very low, the artifact in the RV was large in this heart, and the overlap of the brightness $\tilde{b}_n(x)$ between the heart wall and lumen was 47.0%. Figure 11(b) shows an image of the MSCF (4.2 MHz, $N = 1$). Figure 11(c) shows the result of region identification. Although there was misclassification around the aorta (Ao), the IVS was clearly differentiated from the RV and the LV.

4. Discussion

4.1 Relationship between phase variance and MSCF

The possibility of misclassification is the smallest at frequency $2f_\mathrm{p}$ as described in §3.3. In this section, the reason is discussed using the relationship between the variance in phase variations and the MSCF.

In the analyzed period (100 frames), a larger variance $\sigma_\phi^2(f)$ of the phase variation $\Delta\phi_n(f)$ between the spectra

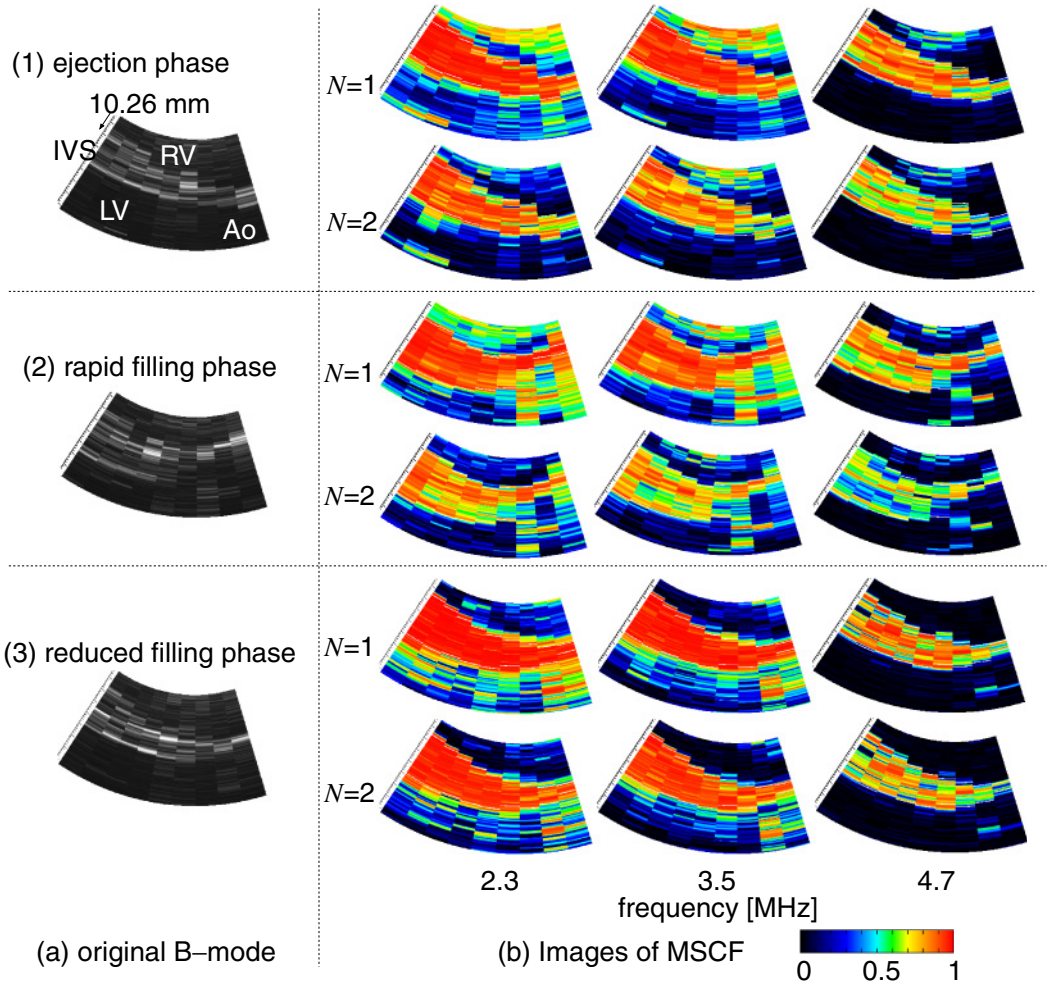

Fig. 7. (Color online) (a) Original B-mode images. (b) Images of MSCF $|\gamma_x(f)|^2$ at each frequency in 3 cardiac phases. Color codes are the same as those in Fig. 6(b).

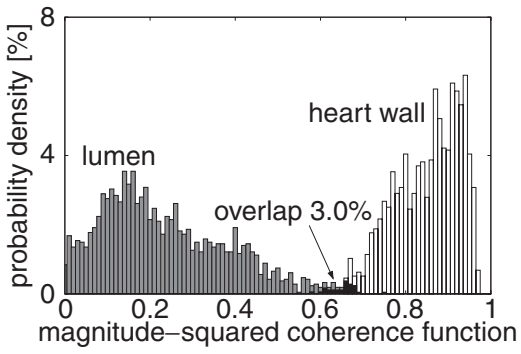

Fig. 8. Histograms of MSCF $|\gamma_x(f)|^2$ (frequency: 4.2 MHz, $N = 1$) in heart wall and lumen acquired from 9 beams. In this analysis, the region near the anterior wall (<10.26 mm), in which the artifact was dominant, was not included.

$\hat{Y}_{2n,x}(f)$ and $\hat{Y}_{2n+N,x}(f)$ in $(2n)$-th and $(2n+N)$-th frames leads to a lower MSCF. The phase variation $\Delta\phi_n(f)$ is shown as follows:

$$\Delta\phi_n(f) = \arg[\hat{Y}^*_{2n,x}(f)\hat{Y}_{2n+N,x}(f)], \tag{4.1}$$

The relationship between the standard deviation of the $\sqrt{\sigma^2_\phi(f)}$ of the phase variation $\Delta\phi_n(f)$ between the spectra $\hat{Y}_{2n,x}(f)$ and $\hat{Y}_{2n+N,x}(f)$ and MSCF $|\gamma_x(f)|^2$ was simulated under the assumption that the power spectrum does not vary with time but only the phase varies. The distribution of $\Delta\phi_n(f)$ was assumed to be Gaussian whose average is zero deg, as shown in Fig. 12(a). The number of $[\hat{Y}^*_{2n,x}(f)\hat{Y}_{2n+N,x}(f)]$ was set at 10,000, which is sufficient for obtaining smooth graphs. Figure 12(b) shows the result of simulation to estimate the relationship between $\sqrt{\sigma^2_\phi(f)}$ and $|\gamma_x(f)|^2$. When it is assumed that the phase of the RF signal depends on the location of scatterers, $\Delta\phi_n(2f_p)$ is twice $\Delta\phi_n(f_p)$ and also $\sqrt{\sigma^2_\phi(2f_p)}$ is twice $\sqrt{\sigma^2_\phi(f_p)}$ because $\Delta\phi_n(f)$ occurs owing to the displacement of scatterers. Therefore, when $\sqrt{\sigma^2_\phi(f_p)}$ is as small as 10°, as is expected in the heart wall, $|\gamma_x(f_p)|^2$ is 0.95 and $|\gamma_x(2f_p)|^2$ is 0.8. On the other hand, when $\sqrt{\sigma^2_\phi(f_p)}$ is 30°, as is expected in the lumen, $|\gamma_x(f_p)|^2$ is 0.6 and $|\gamma_x(2f_p)|^2$ is significantly decreased to 0.15. Therefore, the ratio between the MSCF in the heart wall and the lumen at $2f_p$ is larger than that at f_p.

Figure 13 shows the distribution of the phase variation $\Delta\phi_n(f)$ in *in vivo* data obtained from regions (β), (γ), (δ), and (ε) in the rapid filling phase shown in Fig. 4(b). Figures 13(a) and 13(b) show the results at 2.3 MHz ($\approx f_p$) and 4.5 MHz ($\approx 2f_p$), respectively. From these results, the assumption that the distribution of $\Delta\phi_n(f)$ is Gaussian whose average is zero deg is shown to be adequate. Therefore, the complex coherence function $\gamma_x(f)$ was not employed but the MSCF $|\gamma_x(f)|^2$ was employed in this study

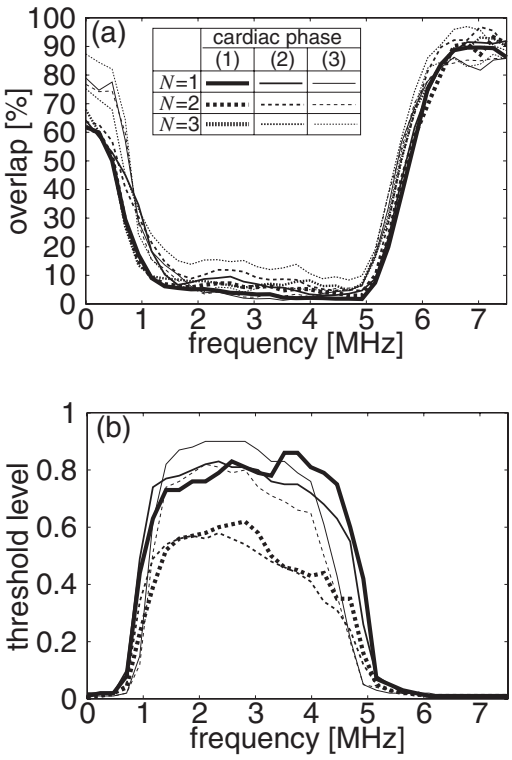

Fig. 9. (a) Overlaps of MSCF $|\gamma_x(f)|^2$ between heart wall and lumen. (b) Optimal threshold levels $T_0(f)$ of MSCF $|\gamma_x(f)|^2$ determined by MSCFs in manually assigned heart wall and lumen. (1) Ejection phase. (2) Rapid filling phase. (3) Reduced filling phase.

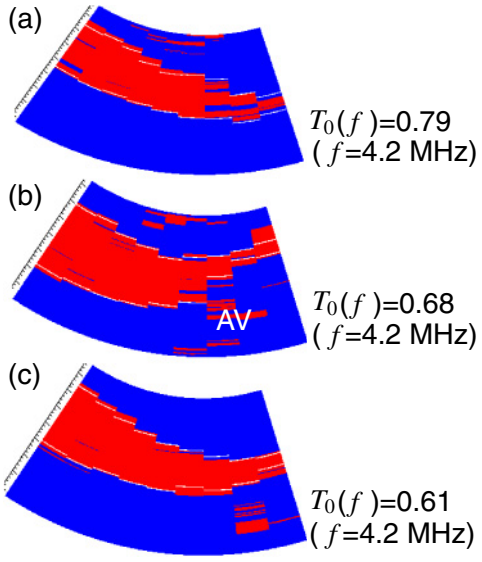

Fig. 10. (Color online) Region identification using optimal threshold determined in Fig. 9(b). (a) Ejection phase. (b) Rapid filling phase. (c) Reduced filling phase.

because the phase of $\gamma_x(f)$ is 0° when the average of $\Delta\phi_n(f)$ is zero deg and echo amplitude is constant along the direction of frame.

4.2 *Relationship between N and MSCF*

The possibility of misclassification is the smallest when $N = 1$ as described in §3.3. In this section, the relationship between N and the MSCF is discussed using the relationship

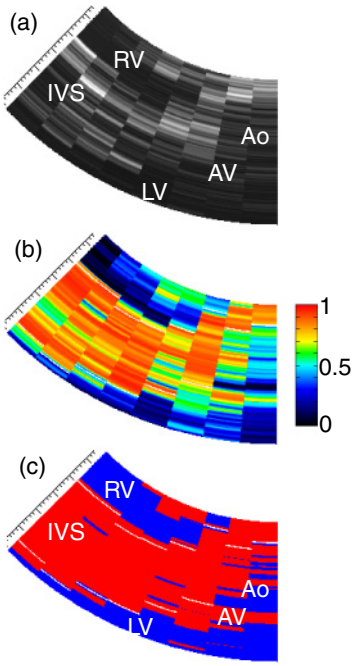

Fig. 11. (Color online) Results for 24-year-old male. (a) Original B-mode image. (b) Image of MSCF in rapid filling phase (4.2 MHz, $N = 1$). (c) Region identification using optimal threshold [$T_0(f) = 0.47$, $f =$ 4.2 MHz].

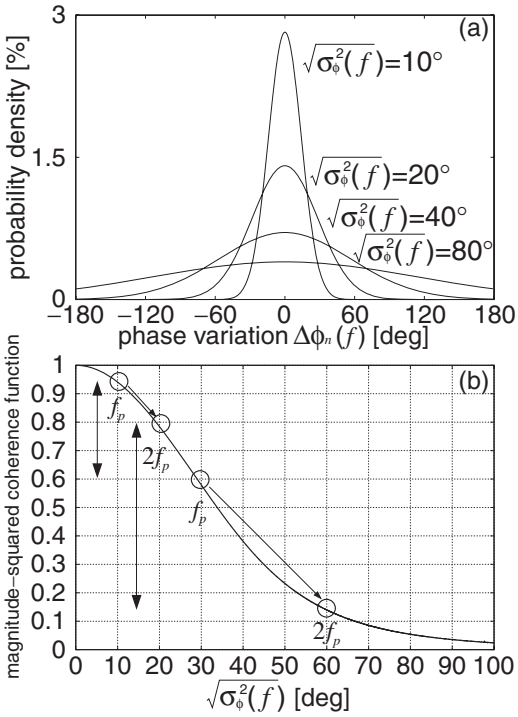

Fig. 12. (a) Gaussian distribution. (b) Simulation of relationship between magnitude-squared coherence function $|\gamma_x(f)|^2$ and standard deviation $\sqrt{\sigma_\phi^2(f)}$ of phase variation $\Delta\phi_n(f)$ between spectrum $\hat{Y}_{2n,x}(f)$ in $2n$-th frame and $\hat{Y}_{2n+N,x}(f)$ in $(2n + N)$-th frame.

between blood flow velocity and the MSCF and that between the change in thickness of the myocardia and the MSCF.

The maximum blood flow velocity in the LV measured by the ultrasonic Doppler method was about 0.7 m/s in the rapid filling phase [Fig. 14(a)]. The ultrasonic beam

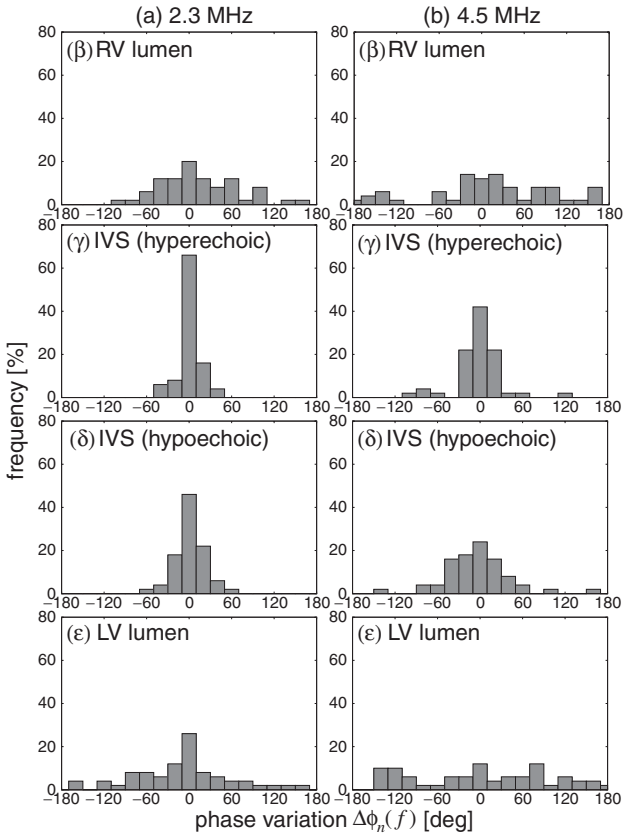

Fig. 13. Distribution of phase variation $\Delta\phi_n(f)$ between spectra in $(2n)$-th and $(2n+N)$-th frames ($N=1$). (a) 2.3 MHz. (b) 4.5 MHz.

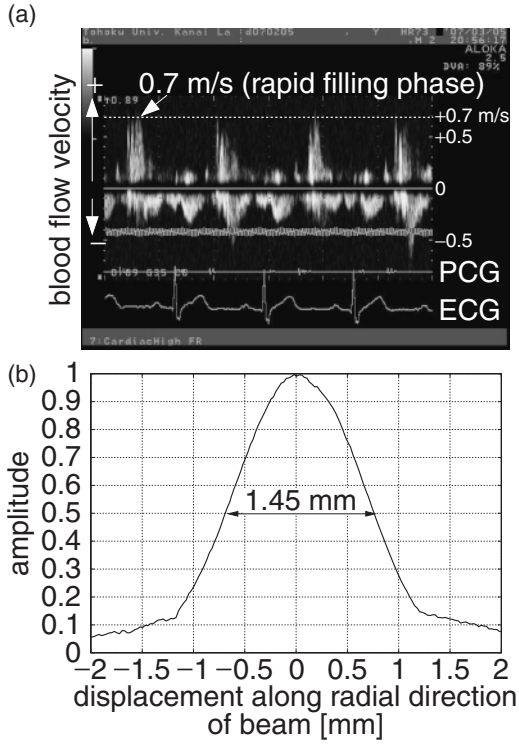

Fig. 14. (a) Blood flow velocity in LV measured by ultrasonic Doppler method. (b) Maximum of amplitude of echo from fine wire. Ultrasonic beam width was determined by width at half maximum.

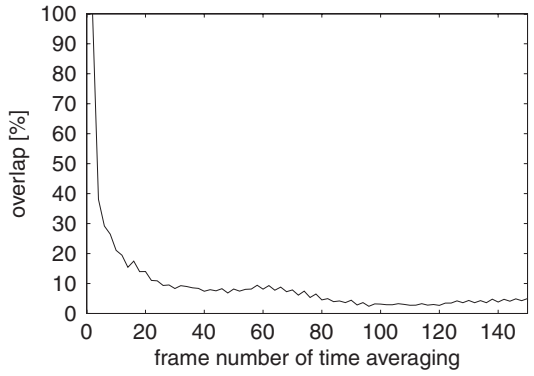

Fig. 15. Relationship between %overlap of MSCF and frame number of time averaging.

diameter measured as a width at half maximum of the amplitude of an echo from a fine metal wire was 1.45 mm [Fig. 14(b)]. Therefore, blood cells may completely slip off from the beam during 2 ms (1.2 frames) in the rapid filling phase. That is why, in the lumen, the MSCF is slightly high when $N=1$ but is almost zero when $N=2$ in the cardiac phases in which blood flow is fast as in the ejection and rapid filling phases. In the reduced filling phase, the MSCF in the lumen is also slightly high when $N=2$ because blood flow is slow (<0.3 m/s) and the scatterers stay in the same focal area of the beam during a few frames. On the other hand, in the IVS, the MSCF also decreases in the ejection and rapid filling phases when N is increased because the number and thickness of myocardial fibers included in an analyzed window varies during N frames. In the reduced filling phase, the MSCF in the heart wall does not decrease markedly when N is increased because the number and thickness of myocardium fibers included in a analyzing window does not vary markedly during N frames. Therefore, the optimal threshold levels of the MSCF are almost the same in three cardiac phases when $N=1$ but those in the ejection and rapid filling phases are much lower than that in the reduced filling phase when $N=2$, as shown in Fig. 9(b). Moreover, in Fig. 9(a), %overlaps of the MSCFs in the heart wall and lumen at $N=1$ are smaller than those at $N=2$ in the ejection and rapid filling phases because the decrease in the MSCF owing to the increase in N in the heart wall is larger than that in the lumen. Therefore, in this study, the optimal value of N was determined to be $N=1$.

4.3 Number of frames in time averaging

In eq. (2.5), the number of frames in time averaging was set to be 100 frames. This setting is shown to be appropriate as described below.

Figure 15 shows the relationship between the %overlap of the MSCF and the number of frames in time averaging. A small number of frames in time averaging would take a large MSCF also in the lumen. On the other hand, a large number of frames in time averaging would take a small MSCF in the heart wall because of the large change in the echo signal $\sigma_\phi^2(f)$ owing to a large change in the thickness of the myocardia during the averaging period. When the number of frames in time averaging is about 100, %overlap becomes the smallest, as shown in Fig. 15. Therefore, in this study, 100-frame averaging was employed.

5. Conclusions

On the basis of the evaluation of the temporal changes in the frequency spectra of RF echoes from the heart using the magnitude-squared coherence function, the difference between time changes of echoes from the heart wall and lumen was shown. Differentiation of the heart wall from the lumen was improved by artifact reduction and use of the high frequency components (at $2f_p$). The possibility of an automated region identification of the heart wall using the magnitude-squared coherence function was shown by the *in vivo* experimental results that the heart wall can be clearly differentiated from the lumen when the optimal threshold for the magnitude-squared coherence function is determined.

1) F. H. Netter: *The Ciba Collection of Medical Illustrations Heart* (Ciba-Geigy Japan, Takarazuka, 1975) pp. 22–47.
2) H. Kanai, H. Hasegawa, and K. Imamura: Jpn. J. Appl. Phys. **45** (2006) 4718.
3) H. Yoshiara, H. Hasegawa, H. Kanai, and M. Tanaka: Jpn. J. Appl. Phys. **46** (2007) 4889.
4) H. Kanai, H. Hasegawa, N. Chubachi, Y. Koiwa, and M. Tanaka: IEEE Trans. Ultrason. Ferroelectr. Freq. Control **44** (1997) 752.
5) M. M. Nillesen, R. G. P. Lopata, I. H. Gerrits, L. Kapusta, H. J. Huisman, J. M. Thijssen, and C. L. de Korte: Ultrasound Med. Biol. **33** (2007) 1453.
6) F. L. Lizzi, M. Greenebaum, E. J. Feleppa, and M. Elbaum: J. Acoust. Soc. Am. **73** (1983) 1366.
7) F. L. Lizzi, M. Ostromogilsky, E. J. Feleppa, M. C. Rorke, and M. M. Yaremko: IEEE Trans. Ultrason. Ferroelectr. Freq. Control **34** (1987) 319.
8) R. J. Watson, C. C. McLean, M. P. Moore, T. Spencer, D. M. Salter, T. Anderson, K. A. A. Fox, and W. N. McDicken: Ultrasound Med. Biol. **26** (2000) 73.
9) K. R. Waters, S. L. Bridal, C. Cohen-Bacrie, C. Levrier, P. Fornès, and P. Laugier: Ultrasound Med. Biol. **29** (2003) 1521.
10) C. S. Hall, E. D. Verdonk, S. A. Wickline, J. E. Perez, and J. G. Miller: J. Acoust. Soc. Am. **101** (1997) 563.
11) G. Georgia and F. S. Cohen: IEEE Trans. Ultrason. Ferroelectr. Freq. Control **48** (2001) 355.
12) G. Georgia, F. S. Cohen, C. W. Piccoli, F. Forsberg, and B. B. Goldberg: IEEE Trans. Ultrason. Ferroelectr. Freq. Control **48** (2001) 364.
13) H. Kanai: IEEE Trans. Ultrason. Ferroelectr. Freq. Control **52** (2005) 1931.
14) H. Kanai, M. Sato, Y. Koiwa, and N. Chubachi: IEEE Trans. Ultrason. Ferroelectr. Freq. Control **43** (1996) 791.
15) H. Kanai: *Spectrum Analysis of Sound and Vibration* (Corona, Tokyo, 1999) p. 97.
16) R. J. Schalkoff: *Pattern Recognition: Stastical, Structual and Neural Approaches* (John Wiley & Sons, New York, 1992) p. 298.